J. Fluid Mech. (2014), *vol.* 752, *pp.* 266–281. © Cambridge University Press 2014
doi:10.1017/jfm.2014.332

Ellipsoidal drop impact on a solid surface for rebound suppression

Sungchan Yun and Geunbae Lim†

Department of Mechanical Engineering, Pohang University of Science and Technology (POSTECH), 77 Cheongam-ro, Nam-gu, Pohang 790-784, Republic of Korea

(Received 28 November 2013; revised 18 March 2014; accepted 8 June 2014; first published online 4 July 2014)

Non-axisymmetric drops can significantly alter impact dynamics via rebound suppression when compared to axisymmetric drops. In this study, we focus on ellipsoidal drop impact on a non-wetting surface and investigate the effects of the geometric aspect ratio (AR) and the Weber number (We) on the dynamics and outcomes of impacts, both experimentally and numerically. Non-axisymmetric spreading features are characterized by scrutinizing the maximal extensions along the x-axis (D_{mx}) and y-axis (D_{my}) with respect to AR and We. The ratio of the maximal extensions depends strongly on AR, following our scaling relation $D_{mx}/D_{my} \sim AR^{1/2}$. Experimental and numerical studies show that increasing AR induces a high degree of axis switching during retraction, thereby resulting in the prevention of drop rebound, where axis switching denotes alternate expansion and contraction along the principal axes. We determine the transition between rebound and deposition (rebound suppression) over the AR and We domains and discuss the transition based on a non-axial distribution of the kinetic energy. The understanding of ellipsoidal drop impacts will potentially provide applications to surface patterning, cleaning, and cooling.

Key words: drops, interfacial flows (free surface)

1. Introduction

The control of drop deposition is an essential issue in a wide range of scientific and industrial communities, such as inkjet printing (de Gans, Duineveld & Schubert 2004), spray coating (Aziz & Chandra 2000), spray cooling (Kim 2007; Deng & Gomez 2011) and pesticide deposition (Wirth, Storp & Jacobsen 1991). For these applications, the efficient deposition of drops with low viscosity and high surface tension, such as water drops, on non-wetting surfaces is challenging because the drops retract violently after impact and subsequently rebound off the surfaces (Rioboo, Tropea & Marengo 2001; Rioboo, Marengo & Tropea 2002; Yarin 2006; Marengo *et al.* 2011). The rebound limits drop deposition, thus leading to material loss, increased spraying costs, or environmental pollution for pesticide spraying (Wirth *et al.* 1991; Bergeron *et al.* 2000).

† Email address for correspondence: limmems@postech.ac.kr

https://doi.org/10.1017/jfm.2014.332 Published online by Cambridge University Press

Drop rebound is governed both by material properties, such as density (ρ), surface tension (σ), and viscosity (μ), and by physicochemical properties, such as surface adhesion and roughness. The key parameters can be organized into the following dimensionless groups: the Weber number ($We = \rho D_0 U_0^2/\sigma$), which represents the ratio of the inertial force to surface tension; the Reynolds number ($Re = \rho D_0 U_0/\mu$), which denotes the ratio of the inertial force to the viscous force; the Ohnesorge number ($Oh = \mu/(\rho\sigma D_0)^{1/2}$), which indicates the ratio of the viscous force to the inertial and surface tension forces, where D_0 and U_0 are the effective diameter and impact velocity, respectively. Mao, Kuhn & Tran (1997) modelled rebound as a function of the maximum spreading factor and surface wettability. Rioboo *et al.* (2001) investigated several parameters involved in drop rebound and found scenarios of rebound for increasing impact velocity, increasing surface tension, or increasing receding angle. Reyssat *et al.* (2006) and Rioboo *et al.* (2008) analysed the velocity-dependent behaviour of drops impacting upon superhydrophobic surfaces, based on a minimal impact velocity for drop rebound varying as $U_c \sim (\sigma/\rho D_0)^{1/2}$, derived from the kinetic energy (KE) ($\sim\rho D_0^3 U_0^2$) exceeding the surface energy ($\sim\sigma D_0^2$). Biance *et al.* (2006) reported that, for elastic shocks upon heated and superhydrophobic walls, the size of the drop being smaller than the capillary length ($(\sigma/\rho g)^{1/2}$) is a criterion for rebound, regardless of the impact velocity. Antonini *et al.* (2013) proposed that the receding contact angle being greater than 100° plays a dominant role in drop rebound, compared with other factors such as contact angle hysteresis, surface roughness and the Weber number.

Several methods have been proposed to improve drop deposition and suppress rebound, including adding chemical agents and modifying target surfaces. Polymer additives in low-viscous drops significantly alter the impact behaviour and inhibit rebound by intervening in fluid rheology (Bergeron *et al.* 2000; Bartolo *et al.* 2007; Smith & Bertola 2010). Small amounts of particles with polymer additives dampen the rebound by increasing the frictional force at the substrate (Zang *et al.* 2013). Surfactant additives are used to prevent rebound and liquid column fracture during retraction by changing the wetting properties (Mourougou-Candoni *et al.* 1997; Crooks, Cooper-Whitez & Boger 2001; Aytouna *et al.* 2010; Gatne, Jog & Manglik 2009). The presence of an electric charge on drops affects the impact behaviour by pinning drops on heated conducting surfaces, thereby hindering drop rebound (Deng & Gomez 2010, 2011). An electrowetting phenomenon can stick drops to dielectrics coated on electrodes, without rebound, by controlling wettability (Lee *et al.* 2013). Drop rebound can be promoted or suppressed by using the target motion of a solid substrate (Lee & Kim 2004). Surface elasticity, such as a stretchable polymer film, can suppress rebound because the initial energy is partially used to deform the substrate (Mangili *et al.* 2012; Cho *et al.* 2013).

Recently, it has been reported that a non-axisymmetric shaped drop can effectively suppress drop rebound without the use of additives or target solid modification (Yun, Hong & Kang 2013). The experimental observations showed that a non-axisymmetric drop alternately spreads and retracts along the horizontal principal axes after impact, thereby weakly inducing a vertical (axial) elongation of the drop. Numerical analyses of drop impact rationalized the effect of the drop shape on impact dynamics by reproducing axis switching during the retraction process, where axis switching denotes alternate expansion and contraction along the horizontal axes. However, the previous work presented the criteria of the impact velocity for rebound suppression without controlling the drop shape. Furthermore, knowledge of the shape-dependent suppression mechanism was insufficient for use in practical applications. Therefore,

https://doi.org/10.1017/jfm.2014.332 Published online by Cambridge University Press

the effect of the drop shape on the behaviour and outcome of the impact should be further investigated.

In this work, we focus on ellipsoidal drop impact on a smooth, non-wetting surface and scrutinize the effect of the geometric aspect ratio (*AR*) and Weber number (*We*) on the dynamics and outcome of the impact both experimentally and numerically. For varying *AR*s, the impact behaviour obtained from the simulation is compared with that obtained from experiment. The non-axisymmetric spreading dynamics is characterized in terms of the maximal extension for each principal axis by a simple scaling analysis, which is verified by the experimental and numerical data. We suggest the critical *AR* and *We* values wherein drop rebound is suppressed and discuss the transition between rebound and deposition (rebound suppression) by conducting quantitative analyses on a non-axial distribution of KE. This work considers *AR* at the impact point ranging from 1.0 to 2.0 and the impact velocity ranging from 0.5 to 1.6 m s^{-1}, which yields *We* ranging from 7 to 70, *Re* ranging from 990 to 3150 and *Oh* of 0.0027. In the given ranges, the viscous force is negligible; thus, both the inertial and surface forces can govern the impact dynamics.

2. Experimental setup

Ellipsoidal drops were produced by using a typical nozzle-ring electrospray device where the ring electrode has an elliptic hole (figure 1*a*). The ring was made of copper and had an outer diameter and thickness of 20 and 2 mm, respectively. The elliptic hole had major and minor axes of 12.5 and 6.5 mm, respectively. The distance between the nozzle and ring was 2 mm. A DC voltage of 6 kV was applied to the electrodes for 10 ms as a pulse, which was the optimal condition for the efficient detachment and maximal deformation of a single drop. The electric signal applied to the drops was produced by a function generator (Agilent, 33220A) and a high-voltage amplifier (Trek, 10/10B). Distilled water was used as a working fluid, wherein the surface tension was measured as 71.8 ± 0.3 mN m^{-1} by using a tensiometer (Lauda TD2), and was provided through the stainless-steel nozzle (Hamilton, 27 gauge) by a syringe pump. When a single drop hung from the nozzle with a fixed volume ($\sim$4 μl), the signal was applied. The signal was turned off when the impinging drop passed through the ring. The falling drops impacted with a Teflon-coated (DuPont, AF1600) glass. The static contact angle on the surface was measured as $116 \pm 3°$. The impact velocity of the drop was controlled by adjusting the falling distance from the nozzle to the substrate. To obtain various *AR*s of the drop at a constant impact velocity, we attempted to adjust the falling height very slightly or adjust a gap between the needle electrode and the ring electrode very slightly. We captured the bottom and side views of the impact behaviour of drops separately by using a high-speed camera (Photron, Fastcam SA3) with capturing speeds of up to 10 000 f.p.s. and shutter speeds of down to $30\,000^{-1}$ s.

The volume of the drop and amount of electric charge were consistent in this work. The volume of a single drop was estimated to be 4.0 ± 0.1 μl by measuring the weight of several drops. The charge quantity of a single drop was measured to be 0.30 ± 0.01 nC by collecting the drop in a Faraday cup connected to an electrometer (Keithley 6514) inside a Faraday cage. An axisymmetric (spherical) drop was non-electrostatically produced by dripping from the nozzle (Hamilton, 33 gauge), wherein the measured volume was 3.9 ± 0.1 μl. The effect of the electric charge of the drop on the impact dynamics and the outcome was negligible, according to our previous experimental study (Yun *et al.* 2013).

https://doi.org/10.1017/jfm.2014.332 Published online by Cambridge University Press

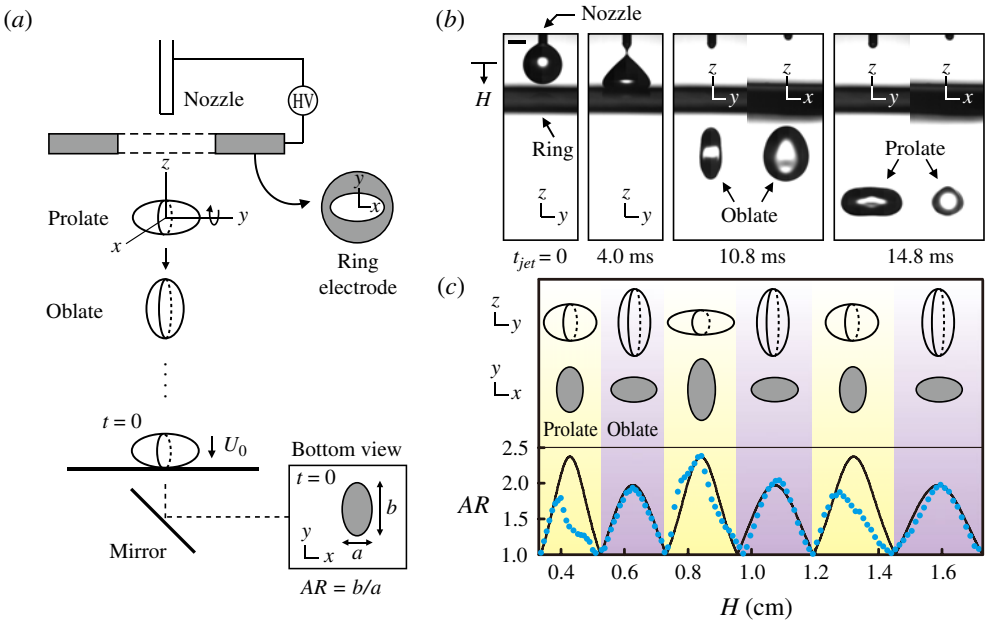


FIGURE 1. (Colour online) (*a*) Schematic (not to scale) of the experimental set-up to observe the impact behaviour of a drop with *AR*. (*b*) Drop deformation into an ellipsoidal shape by electric field applied at $t_{jet} = 0$ ms; the scale bar is 1 mm. (*c*) The variation of *AR* with respect to *H*, the falling distance from the nozzle to the drop centre; the symbol and line correspond to the estimated *AR* from the side-view experiment and theoretical *AR*, respectively. Insets indicate the schematic side and bottom views of the shape oscillation alternating between oblate and prolate ellipsoids, which are axisymmetric with respect to the *y*-axis.

The deformation of the drop into an ellipsoidal shape occurred as follows: (*a*) when the electric field was applied, the drop hanging from the nozzle begun to stretch vertically and pinched off (figure 1*b*), thereby inducing a longitudinal oscillation; (*b*) the drop was also non-axisymmetrically deformed near the ring, because a narrower gap in the elliptic hole exerts a stronger electric force on the drop, thus causing transverse (horizontal) oscillation; (*c*) when the initial ellipsoidal shape was created, the drop oscillated longitudinally and transversely with a period of ∼9 ms. For a detailed description, see the experimental observations of Yun *et al.* (2013).

Shape oscillation can be approximately represented by Laplace's spherical harmonics (Rayleigh 1879; Lamb 1945), thus providing a radius of $r(t, \phi) = r_0[1 + \zeta \cos(wt)P_2(\cos\phi)]$, where $\zeta = 0.48$ and $f = w/2\pi = 120.1$ Hz are fitting parameters, $P_2(x) = (3x^2 - 1)/2$ is the Legendre polynomial of the second degree, and ϕ is the azimuthal angle. The oscillation frequency is close to 120.8 Hz, obtained from the inviscid Rayleigh theory value of $f_D = (4/\pi)[\sigma/(\rho D_0^3)]^{1/2}$ (Rayleigh 1879). The modal shape is axisymmetric with respect to the *y*-axis but is non-axisymmetric with respect to the *z*-axis and normal to the substrate. The non-axisymmetry of the drop is expressed as *AR*, a proportion between the major and minor axes of the horizontal cross section. We measured accurate values of *AR* from the bottom-view experiments in many cases. The estimated *AR* were additionally obtained from the side-view experiments to plot *AR* versus the falling distance in figure 1(*c*), along with

https://doi.org/10.1017/jfm.2014.332 Published online by Cambridge University Press

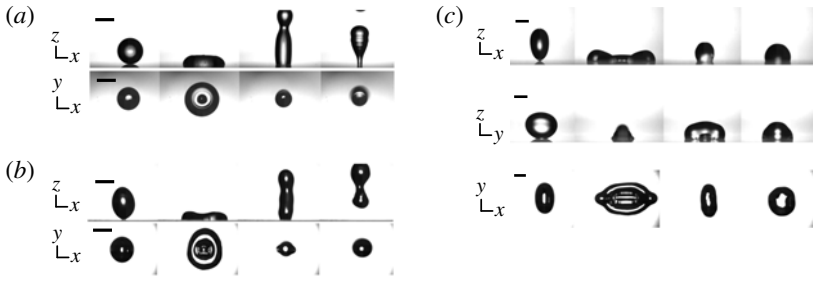


FIGURE 2. Impact behaviours for three distinct cases at the same impact velocity ($We = 30$): (a) a spherical drop, (b) a slightly deformed ellipsoidal drop ($AR = 1.10$), and (c) a highly deformed ellipsoidal drop ($AR = 1.60$); time proceeds in each row at 5 ms intervals. The scale bar is 1 mm.

the theoretical AR given by $\alpha = r(t, 0)/r(t, \pi/2) = [1 + \zeta \cos(wt)]/[1 - (\zeta/2)\cos(wt)]$. This work defines $AR \geqslant 1.0$; thus, AR corresponds to α^{-1} if $\alpha < 1.0$ (oblate ellipsoid). The discrepancy between the experimental and theoretical AR might be due to the superimposed mode with longitudinal oscillation in the experiment.

As for the geometrical effects on drop impact, for identical AR, the impact behaviour of the oblate drop is only slightly different from that of the prolate drop. We proved the result in the online supplementary materials (§ S1) available at http://dx.doi.org/10.1017/jfm.2014.332. The amplitudes of the oscillation will diminish due to viscous dissipation at a rate of $\exp(-t/\tau_v)$, where $\tau_v = \rho D_0^2/(20\mu) = 0.19$ s (Lamb 1945). Given the longest falling time of 0.12 s, the damping effect can reduce the amplitudes by 46 %. In the experiment, we obtained the minimal peak AR of 1.75. The impact behaviour of a spherical drop was compared with that of the ellipsoidal drop to understand the effect of AR (figure 2).

3. Numerical method

We investigated the impact dynamics of ellipsoidal drops by conducting a three-dimensional numerical simulation using the volume of fluid method. This method is widely used in drop simulation to track the interface dynamics while inherently conserving mass. Our numerical scheme is totally based on previous works that analyse drop impact on a solid surface (Gunjal, Ranade & Chaudhari 2005; Lunkad, Buwa & Nigam 2007). The grid resolution of the drop was 14 cells per radius (∼1 mm) and is more refined near the substrate. We employed a time step of 1 μs and a maximum internal iteration of 30 per time step, which is suitable for normalized residuals less than 10^{-5}.

The ellipsoidal drop shape was initially patched in the simulation domain and governed by the standard equation, $x^2/(a_0/2)^2 + y^2/(b_0/2)^2 + z^2/(a_0/2)^2 = 1$, where a_0 and b_0 are the minor and major axes of the cross section of the prolate ellipsoid, respectively; the major axis (y) is parallel to the substrate. We chose both a_0 and b_0 to obtain the desired AR between 1.0 and 2.0 at the moment of impact. For liquids, a water drop ($\rho = 1000$ kg m^{-3}; $\mu = 1$ mPa s) with 4 μl volume was surrounded by air ($\rho = 1.21$ kg m^{-3}; $\mu = 1.81 \times 10^{-2}$ mPa s). Interfacial tensions of 72, 50, and 28 mN m^{-1} were used. The impact velocity (0.5–1.5 m s^{-1}) was applied to the drop levitated at the corresponding position. The ellipsoidal drop impact exhibited complicated contact angle dynamics where advancing and receding concurrently occur

https://doi.org/10.1017/jfm.2014.332 Published online by Cambridge University Press

in the contact line. The impact dynamics can be economically represented by using the average contact angle in the simulation, similar to the work of Gunjal *et al.* (2005). A contact angle of 100° is adequate as a boundary condition at the solid wall because the model can reproduce the experimental data of the temporally resolved contact widths for each axis. The model can predict the maximal extension during spreading within an accuracy of 5 %. Model validation is further discussed in the supplementary material (§ S2).

4. Results and discussions

4.1. *Impact dynamics of ellipsoidal drops*

We start from experimental observations of the drop impact for different *AR*s. The effective drop diameter and impact velocity were $D_0 = 1.97$ mm and $U_0 = 0.94$ m s^{-1}, respectively, which yielded $We = 23$, $Re = 1790$ and $Oh = 0.0027$. Hence, the viscous force is negligible and the impact dynamics of drops depend mainly on a capillary–inertia balance. The crashing time τ_{cra}, which is the time for drops to spread entirely on a surface, is of the order of D_0/U_0. Before impacting, drops oscillate with a time period τ_{osc} that is of the order of $(\rho D_0^3/\sigma)^{1/2}$. We can realize the effect of the oscillation on the impact behaviour from the ratio of time scales $\tau_{osc}/\tau_{cra} = We^{1/2}$. This implies that the drop oscillation only slightly affects the impact behaviour at high *We* because the shortest time is dominant. This is proven in the supplementary materials (§ S1). Therefore we expect to observe impact behaviour driven mainly by *AR* in this experiment ($We < 70$). Figure 2 demonstrates the dominant effect of *AR* on impact behaviour and shows that an ellipsoidal drop ($AR = 1.60$) suppressed drop rebound, whereas a nearly axisymmetrical ellipsoidal drop ($AR = 1.10$) rebounded off the substrate, similar to a spherical drop.

Figure 3 shows the impact behaviour for three different *AR*s. For a low *AR* (figure 3*a*), the drop remained almost axisymmetric during impact, resulting in rebound. The drop with an intermediate *AR* (figure 3*b*) spread by varying the shape into an ellipse and then retracted by aligning itself on the *x*-axis. For a high *AR* (figure 3*c*), the drop expanded more along the *x*-axis than the drop with intermediate *AR*, and then aligned along the *x*-axis. The liquid alignment formed in such a way that rims in the periphery of the lamella merged in a fast retraction along the *y*-axis, as shown at $t = 5.0$–6.9 ms of figure 3(*c*); this process resembles a spherical drop impact upon anisotropic surfaces (Kannan & Sivakumar 2008, figure 10). The liquid aligned with the *x*-axis was released and squeezed outward along the *y*-axis and then completed the second alignment with the *y*-axis, as shown at $t = 12.9$ ms of figure 3(*c*). An alternate expansion and contraction of the drop repeatedly occurred along the *x*-axis and the *y*-axis, which we have called axis switching. The contraction process during axis switching is similar to the capillary retraction of a non-axisymmetric impact-created air cavity in water (Enriquez *et al.* 2012); the retraction accelerates along the longer axis because the radius of curvature is higher at the tips.

To understand axis switching better, in figure 4 we illustrate the spreading and retracting processes of drops for low *AR* (rebound case) and high *AR* (deposition case). The drop begins to spread at $t = 0$ when viewed from a bottom plate. When the half-volume of the drop spreads at $t \sim (1/2)\tau$, a contact line of the drop drawn as a solid line becomes temporarily circular (see also the second frames of the *xy*-plane in figure 3). During this time, the drop reaches its maximal extension in the *y*-axis. The drop continues to spread and becomes an elliptic puddle at $t \sim \tau$ (see also the third frames of the *xy*-plane in figure 3). During this time, the drop reaches maximal

https://doi.org/10.1017/jfm.2014.332 Published online by Cambridge University Press

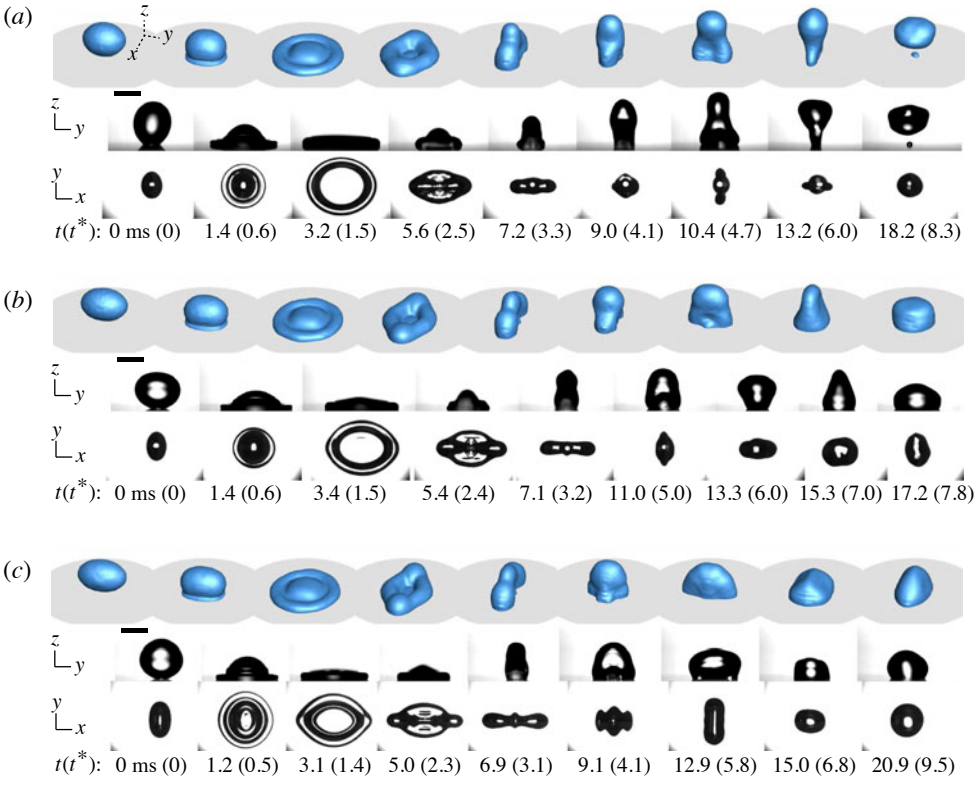


FIGURE 3. (Colour online) Temporal evolution of impacting drops ($We = 23$) obtained from the simulation (uppermost) and side-view and bottom-view experiments (lower) for three AR cases. (a) Rebound occurs when AR is equal to 1.26 (simulation) and 1.20 (experiment). (b) The rebound is suppressed when AR is equal to 1.43 (simulation) and 1.38 (experiment). (c) The rebound is also suppressed when AR is equal to 1.63 (simulation) and 1.62 (experiment). The dimensionless time t^* is defined to be t/τ, where $\tau = D_0/U_0$. The scale bar is 1 mm.

extension in the x-axis. Drops behave differently during retraction depending on the AR. The drop with low AR retracts to the direction of the centre and rarely introduces axis switching at $t \sim \tau$. In contrast, the drop with high AR retracts along the y-axis but spreads along the x-axis at $t \sim \tau$. These phenomena induce the alignment of the liquid on the x-axis and the consequent axis switching without rebounding. The rebound suppression can be explained by the KE consumption in axis switching rather than in converging with the symmetry axis (z-axis) during retraction.

Figure 5 shows the normalized contact widths of drops in the x-axis (D_x/D_0) and y-axis (D_y/D_0). The solid lines and symbols correspond to numerical and experimental results, respectively. The dashed lines represent the temporal variation of the normalized contact diameter of a spherical drop obtained experimentally. The temporal evolution of the widths shown in the simulation and experiment are comparable to each other for any AR case. We observed a slight discrepancy in the contact width and the maximal height between simulation and experiment, which may arise from the complicated contact angle dynamics induced by contact angle hysteresis and contact line friction, which have not been considered in the simulation,

https://doi.org/10.1017/jfm.2014.332 Published online by Cambridge University Press

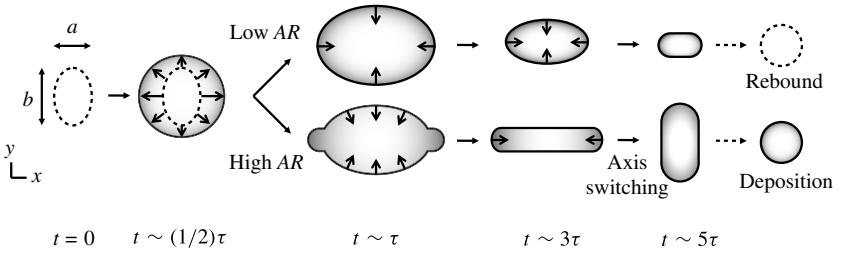


FIGURE 4. Illustration of the spreading and retracting behaviour of a drop in the bottom view for low and high *AR*s, where $AR = b/a$. The solid and dashed lines represent the contact lines on the solid surfaces and the outermost liquid–air interfaces, respectively. The drop begins to spread at $t = 0$. The drop shape becomes circular at $t \sim (1/2)\tau$ and becomes elliptic at $t \sim \tau$, where $\tau = D_0/U_0$. Thereafter, the drop begins to retract. For low *AR*, the drop retracts in the direction of its centre, thus resulting in drop rebound. For high *AR*, the drop retracts along the *y*-axis but spreads along the *x*-axis, thus inducing axis switching without rebound, where axis switching denotes the alternate expansion and contraction of the drop along the *x*- and *y*-axes during retraction.

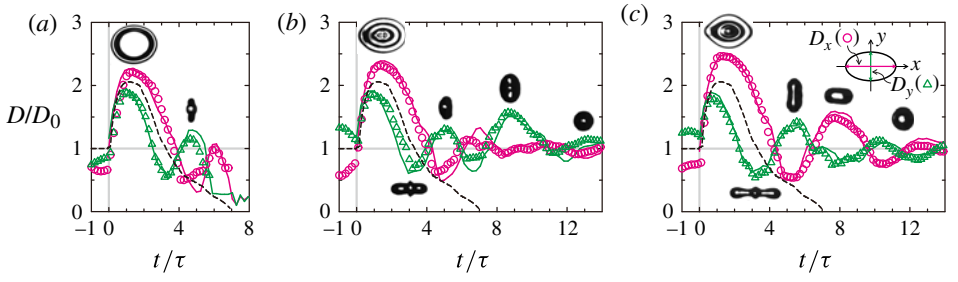


FIGURE 5. (Colour online) (*a*)–(*c*) Temporal evolution of the normalized contact width D/D_0 of drops corresponding to figure 3(*a*–*c*), with increasing *AR*s. Drops begin to spread at $t = 0$. The crashing time τ is equal to D_0/U_0. The symbols denote the experimental results in the *x*-axis (○) and the *y*-axis (△), as described in the upper right corner of (*c*). The solid lines indicate the simulation results in the *x*-axis (pink line) and *y*-axis (green line). The dashed lines represent the temporal variation in the diameters of spherical drops ($AR = 1.0$) obtained experimentally. The standard deviation of the experimental result is within 7 %. Snapshots of the insets represent the bottom views of the impact behaviour obtained experimentally at the corresponding time.

as further discussed in the supplementary material (§ S2). The spreading dynamics indicates that the maximal extensions in the *y*-axis D_{my}/D_0 are found earlier and are smaller than the maximal extensions of the spherical drops, whereas the maximal extensions in the *x*-axis D_{mx}/D_0 are found later and are greater than the maximal extensions of the spherical drops. The difference in the maximal extensions between the *x*-and *y*-axes increases with the *AR*. In the retraction process, the oscillations of the widths of the two axes display an obvious reversed phase with diminishing amplitudes as *AR* increases. Thus axis switching is well developed for high *AR*; see the snapshots of insets in figure 5.

We characterized the spreading behaviour by scrutinizing the maximal extensions in the principal axes as a function of *AR* and *We*. First, we numerically investigated the maximal extensions in the *y*-axis D_{my}/D_0 by varying *AR* and *We*. Figure 6(*a*,*b*)

https://doi.org/10.1017/jfm.2014.332 Published online by Cambridge University Press

Symbols in figure 6	Impact velocity, U_0 (m s^{-1})	Surface tension, σ (mN m^{-1})	$We = \rho D_0 U_0^2/\sigma$	$Ca = \mu U_0/\sigma$
□	0.5	72	7	6.9×10^{-3}
△	0.5	50	10	1.0×10^{-2}
☆	0.7	72	14	9.7×10^{-3}
×	0.5	28	18	1.7×10^{-2}
◯	0.9	72	23	1.2×10^{-2}
▽	0.9	50	32	1.8×10^{-2}
◇	1.3	72	46	1.8×10^{-2}
+	0.9	28	58	3.2×10^{-2}
• (for experiment)	0.5–1.6	72	7–70	6.9×10^{-3}–2.2×10^{-2}

TABLE 1. Numerical conditions in the data of figure 6 and the corresponding Weber number.

show the plots of D_{my}/D_0 versus AR and We, respectively. The numerical data in the plots comprise ARs less than 2.0 and the Weber numbers obtained from several impact velocities (U_0) and surface tensions (σ), as listed in table 1. Thus D_{my}/D_0 decreases with increasing AR but increases with increasing We. The line of best least-squares fit of the simulation data is drawn as a solid line, which shows $D_{my}/D_0 \sim AR^{-0.15\pm0.03}$ (figure 6*a*) and $D_{my}/D_0 \sim We^{0.25\pm0.01}$ (figure 6*b*). The latter follows the scaling law $D_m/D_0 \sim We^{1/4}$ (Clanet *et al.* 2004), which is drawn as a dashed red line in figure 6(*b*).

To estimate the scaling relation for the spreading dynamics in the y-axis, we incorporated an axisymmetric model, wherein drops radially spread with the initial horizontal diameter of b, the initial vertical length of a, the impact velocity of V_0 and reach the maximal extension in the y-axis, as observed at $t \sim (1/2)\tau$ in figure 4. The capillary force is balanced by the inertial force during spreading, which can be governed by Euler's equation neglecting the viscous force. The former can be written as the Laplace pressure gradient tending to form a drop into spherical shape, thus scaling as σ/h^2, where h represents the puddle thickness. The latter can be written as the deceleration of the liquid, thus scaling as $\rho V_0^2/a$ (Clanet *et al.* 2004). Capillary–inertia balance for the model gives us the relation $\sigma/h^2 \sim \rho V_0^2/a$, which implies $\sigma/h^2 \sim \rho U_0^2/b$, from consistency of the initial KE between the model and the original prolate drop with $V_0^2 = (a/b)U_0^2$. The details are described in the supplementary material (§ S3). The relation results in $bD_0/h^2 \sim \rho D_0 U_0^2/\sigma = We$. The drop constitutes a still unperturbed part as a rigid body and a spreading part at $t \sim (1/2)\tau$; during this time, the volume of the spreading part is almost half the total volume ($\sim \pi D_0^3/12$), which approximates to a puddle volume ($\sim \pi D_{my}^2 h/4$). Therefore, $h \sim (1/3)D_0^3 D_{my}^{-2}$. The scaling relation for D_{my}/D_0 can be rewritten as

$$D_{my}/D_0 \sim 3^{-1/2}(D_0/b)^{1/4} We^{1/4} \sim AR^{-1/6} We^{1/4}, \tag{4.1}$$

where $D_0/b = AR^{-2/3}$, which is derived from the volume conservation as follows: $a^2 b/D_0^3 = 1 = (a/D_0)^3 (b/a) = (a/D_0)^3 AR$, for the original prolate drop. When D_{my}/D_0 is normalized by $AR^{-1/6} We^{1/4}$ in our limited ranges, the numerical data shown in figure 6(*a*,*b*) are gathered around one straight line (figure 6*c*). Likewise, our experimental data obtained from arbitrary ARs and Weber numbers, as in table 1, are clustered around another straight line. The discrepancy between simulation and experiment is shown, as discussed earlier.

https://doi.org/10.1017/jfm.2014.332 Published online by Cambridge University Press

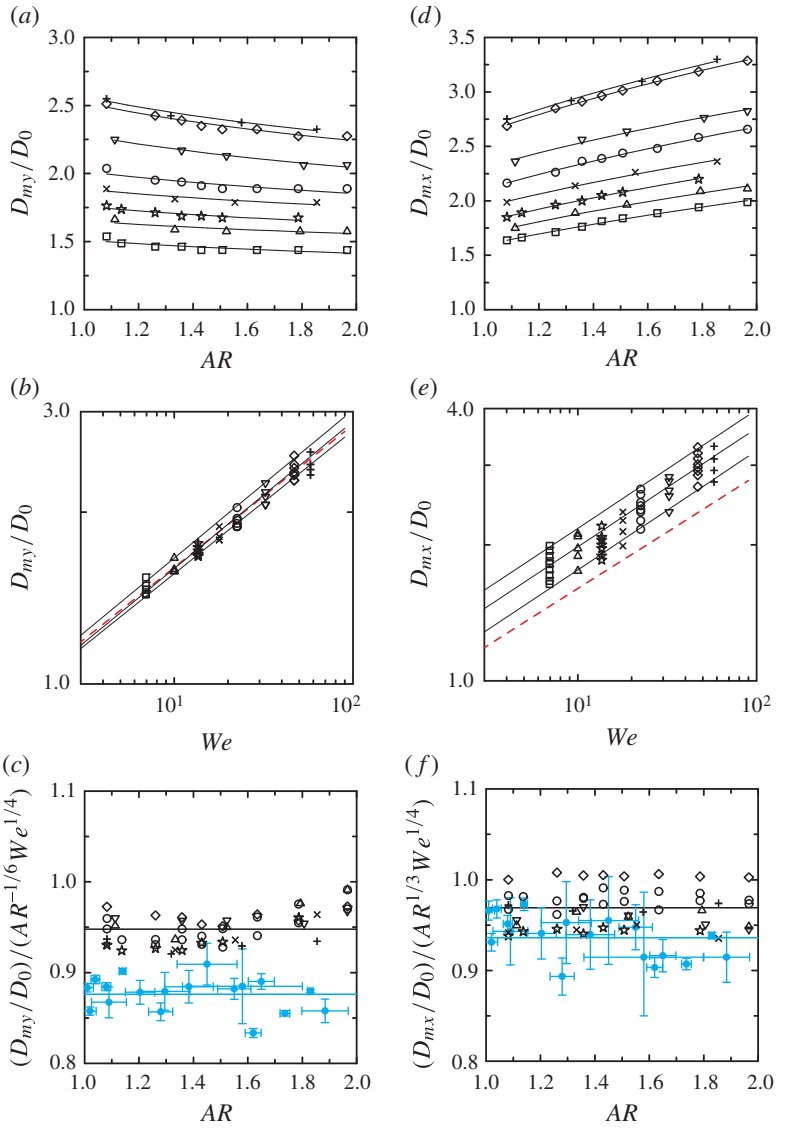


FIGURE 6. (Colour online) The dimensionless maximal extensions in the y-axis D_{my}/D_0 are obtained numerically as a function of (*a*) AR and (*b*) We; the solid lines represent least-squares fits of the simulation data. (*c*) D_{my}/D_0 obtained from simulation and experiment scales as $AR^{-1/6}We^{1/4}$ by (4.1). Similarly to (*a*)–(*c*), the dimensionless maximal extensions in the x-axis D_{mx}/D_0 are obtained numerically as a function of (*d*) AR and (*e*) We; the solid lines represent least-squares fits of the simulation data. (*f*) The ratio D_{mx}/D_0 obtained from simulation and experiment scales as $AR^{1/3}We^{1/4}$ by (4.2). Experimental data (•: blue) are shown only in (*c*) and (*f*). The dashed red line shown in (*b*) and (*e*) correspond to the scaling law $D_m/D_0 = 0.9We^{1/4}$ given by Clanet *et al.* (2004). The solid lines in (*c*) and (*f*) represent the average values of the data. All the symbols are described in table 1.

In accordance with D_{my}/D_0, the numerical results of the maximal extensions in the x-axis D_{mx}/D_0 are plotted in figure 6(*d*,*e*) as a function of AR and We. The whole set of data was obtained from the same numerical and experimental conditions as

https://doi.org/10.1017/jfm.2014.332 Published online by Cambridge University Press

in table 1. The plots indicate that D_{mx}/D_0 increases with AR and We. The lines of best least-squares fit of the simulation data show $D_{mx}/D_0 \sim AR^{0.32\pm0.01}$ (figure 6*d*) and $D_{mx}/D_0 \sim We^{0.26\pm0.01}$ (figure 6*e*). The latter likewise follows the scaling law of Clanet *et al.* (2004), which is drawn as a dashed red line in figure 6(*e*).

We established the scaling relation for the maximal extension in the x-axis. The prolate drop with the initial vertical length of a was assumed to spread by evolving into an elliptic puddle, as observed at $t \sim \tau$ in figure 4. In addition, the maximal extension in the y-axis (D_{my}/D_0) was assumed to hold until $t \sim \tau$, which was used to make the estimation compatible with the scaling relation in the y-axis. We considered the relation $\sigma/h^2 \sim \rho U_0^2/a$ based on a capillary–inertia balance as mentioned earlier, which implies $aD_0/h^2 \sim \rho D_0 U_0^2/\sigma = We$. With a volume conservation between an impinging drop and an elliptic puddle, we obtained $D_0^3 = a^2 b$ and $a^2 b \sim D_{mx} D_{my} h$, which yielded $h \sim D_0^3 (D_{mx} D_{my})^{-1}$. The scaling relation for D_{mx}/D_0 can be rewritten as follows:

$$D_{mx}/D_0 \sim (D_0/a)^{1/2} (D_{my}/D_0)^{-1} We^{1/2} \sim AR^{1/3} We^{1/4}, \tag{4.2}$$

where $D_0/a = AR^{1/3}$ from a volume conservation derived earlier and $D_{my}/D_0 \sim AR^{-1/6} We^{1/4}$ according to (4.1). Figure 6(*f*) indicates that the numerical data shown in figure 6(*d*,*e*) as well as the experimental data are gathered around each straight line when D_{mx}/D_0 is normalized by $AR^{1/3} We^{1/4}$ in our limited ranges. Hence D_{mx}/D_0 are well fitted by the scaling relation, although there is a slight discrepancy in the coefficients of the relations between simulation and experiment. We suggest that the preceding estimations can account for the spreading dynamics in the principal axes as a function of AR and We.

We briefly discuss the coefficients of the scaling relations shown as a straight solid line in figure 6(*c*,*f*). The coefficients can be regarded as dimensional constants dominated mainly by surface wettability in the following relations:

$$D_{mx}/D_0 = C_x AR^{1/3} We^{1/4} \quad \text{and} \quad D_{my}/D_0 = C_y AR^{-1/6} We^{1/4}, \tag{4.3a,b}$$

where C_x and C_y represent the prefactors of the relations of the maximal extensions in the x- and y-axes, respectively. The coefficients were numerically obtained by varying contact angles as boundary conditions ranging from 90° to 160°, which showed that C_x and C_y decrease from approximately 1.0 to approximately 0.7 as the contact angle increases (figure 7). This result agrees with the experimental result showing that the maximal extension decreases with increasing contact angle at $We < 200$ (Antonini, Amirfazli & Marengo 2012). If a drop impacts on a superhydrophobic surface, a slip condition can play a role in minimizing viscous dissipation, which may cause an increase in maximal extension. However, this effect is limited for our regimes because the capillary force greatly affects the spreading dynamics by $We/Re^{1/2} \leqslant 1$ (Pasandideh-Fard *et al.* 1996). More detailed investigation on the effect of surface wettability is beyond the purpose of this work.

4.2. *Criteria for rebound suppression*

The ratio of maximal extensions D_{mx}/D_{my} obtained from simulation and experiment is plotted as a function of AR in figure 8(*a*). The Weber numbers of the simulation are equal to 7, 23, and 46, where $\sigma = 72$ mN m^{-1}, and those of the experiment range from 15 to 50. The plot shows $D_{mx}/D_{my} \sim AR^{0.47}$ for the simulation (solid line) and $D_{mx}/D_{my} \sim AR^{0.46}$ for the experiment (dashed line), which is comparable to $D_{mx}/D_{my} \sim AR^{1/2}$ derived from our scaling relations (4.1) and (4.2). The theoretical

https://doi.org/10.1017/jfm.2014.332 Published online by Cambridge University Press

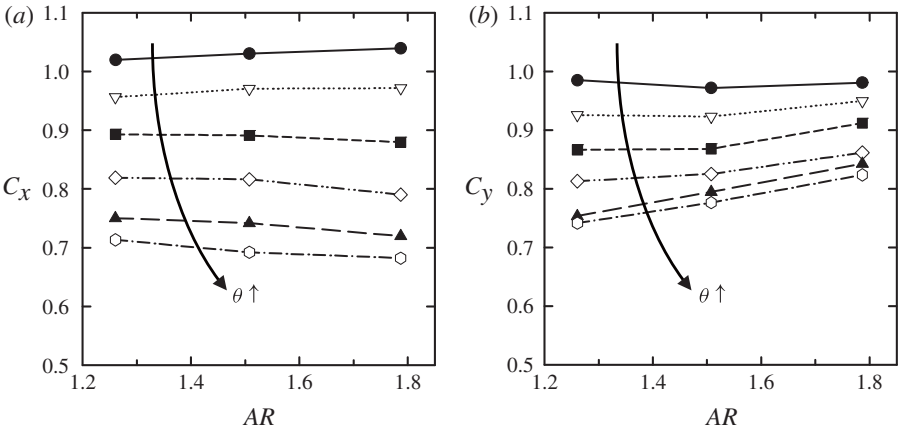


FIGURE 7. Numerical coefficients of (*a*) C_x and (*b*) C_y in (4.3) as a function of *AR*, given contact angles of 90° (●), 100° (▽), 115° (■), 130° (◇), 145° (▲), and 160° (○) in the simulation.

relation suggests that the ratio of maximal extensions is unaffected by *We*. The simulation data show a strong dependence of the ratio on *AR* rather than on *We*, in spite of a slight dependence on *We* at high *AR*.

In figure 8(*a*) we classified the rebound and deposition (rebound suppression) cases using open and filled symbols, respectively. The ratio of the maximal extensions was associated with the rebound/deposition threshold. When D_{mx}/D_{my} is close to 1.2, the rebound regime is distinguishable from the deposition regime. Given $D_{mx}/D_{my} = 1.05AR^{0.47}$ in figure 8(*a*), the critical *AR* was calculated as 1.3, which denotes the lowest value sufficient to suppress drop rebound. The range of *AR* between 1.2 and 1.4 should be a convenient choice for the criterion based on the figure. However, the criterion is still not clearly identified because the effect of the impact velocity is unexplored. For example, we observed from the simulation at $AR = 1.26$ and 1.36 that drop rebound was suppressed for $We = 7$, but was not suppressed for $We = 23$ and 46. Thus the criteria for rebound suppression should be further investigated as a function of both *AR* and *We*.

Figure 8(*b*) shows the transition diagram between the rebound and deposition regimes over the domain of *AR* and *We*, which were obtained experimentally and numerically. The transition is drawn as a dashed curve for the experiment and as a solid curve for the simulation. The curves indicate that *AR* and *We* affect the criteria for rebound suppression and that the growths of the curves increase with increasing *AR* in the experiment and simulation, although the two curves do not converge to one another. We attributed the discrepancy between the curves to the complicated contact angle dynamics in the experiment, which is further discussed in the supplementary material (§ S2). Figure 8(*b*) shows that rebound can be completely suppressed up to $We = 70$ in the experiment for a static contact angle of $116 \pm 3°$, once the drop keeps *AR* more than 1.35. The control of *AR* for rebound suppression is feasible by either adjusting an impinging height to the target surface or deforming a drop shape under the electric field around the impact. When *We* exceeds 70, the transition appears insensitive to *We*, thereby enabling rebound suppression mainly by *AR*.

To explain the transition curves, we introduced a non-axial distribution of KE (η), which denotes a ratio of the non-axial KE to the total KE: $\eta \equiv \int_V (1/2)\rho(u_x^2 +$

https://doi.org/10.1017/jfm.2014.332 Published online by Cambridge University Press

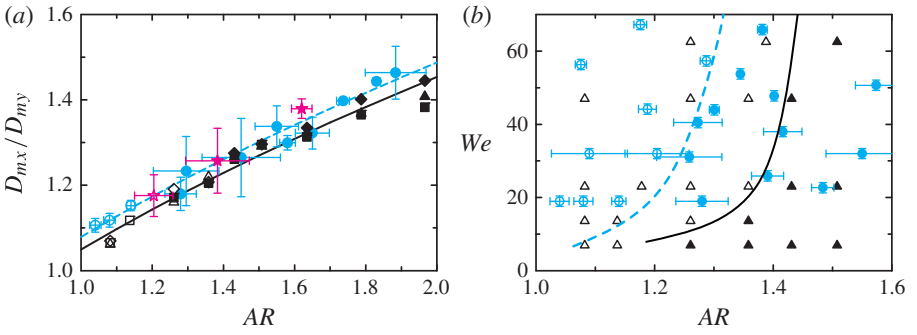


FIGURE 8. (Colour online) (*a*) Ratio of maximal extensions D_{mx}/D_{my} as a function of AR, obtained numerically and experimentally. The least-squares fit shows $D_{mx}/D_{my} \sim AR^{0.47}$ for the numerical data (solid line) and $D_{mx}/D_{my} \sim AR^{0.46}$ for the experimental data (dashed line); the numerical data correspond to $We = 7$ (□), 23 (△), and 46 (◇) where $\sigma = 72$ mN m^{-1}; the experimental data correspond to $We = 15$–50 (○: blue), including the same experiments (☆: pink) shown in figure 3(*a–c*). (*b*) Transition diagram between rebound and deposition (rebound suppression) as a function of AR and We from the simulation (△) and the experiment (○); the solid line (simulation) and dashed line (experiment) are drawn to guide the reader's eye to the transitions. The error bar of the experimental data denotes a standard deviation of AR just before oscillating drops impact on the surface. The static contact angle measured in the experiment is $116 \pm 3°$. The open and filled symbols in (*a*) and (*b*) indicate rebound and deposition cases, respectively.

$u_y^2)\mathrm{d}V/\int_V (1/2)\rho(u_x^2 + u_y^2 + u_z^2)\mathrm{d}V$, where V is the volume of a drop and u_x, u_y, and u_z are the velocity components for each axis. We plotted η as a function of time for various AR in figure 9(*a*). The value of η made no major difference until $t \sim 3\tau$; however, it significantly increased with AR when drops initiated first axis switching at $3\tau < t < 5\tau$.

We also introduced η_s as the value of η measured at the axis-switching time, which can be interpreted as the degree of axis switching; when η_s is close to unity, a high degree of the axis switching develops during retraction. Here, we defined the axis-switching time to be when the contact width of the x-axis first intersects with that of the y-axis, as shown at $t \sim 4.5\tau$ in figure 5 for instance. The axis-switching time can be characterized as a function of AR and We, which is presented in the supplementary material (§ S4).

The value of η_s was fairly closely related to the outcome of the impact. The quantitative study showed that the critical value of η_s can be a crucial factor in representing the actual rebound/deposition transition curves shown in figure 8(*b*). The value of η_s was plotted as a function of AR and We in figure 9(*b*), which showed that η_s increases with increasing AR and saturates to approximately 0.95 at the AR of 1.63, and that η_s decreases with increasing We. We found that the value $\eta_s = 0.77$ can separate the rebound and deposition regimes, which is marked as a dashed line. This indicates that rebound can be suppressed when the non-axial KE is higher than 77 % of the total KE at the axis-switching time. From the contour lines of η_s (inset of figure 9*b*), we were convinced that the transition curve has fairly similar dependence on η_s. The rebound and deposition regimes can also be separated by the critical value of η_s for different surface wettability, which is presented in the supplementary material (§ S5).

https://doi.org/10.1017/jfm.2014.332 Published online by Cambridge University Press

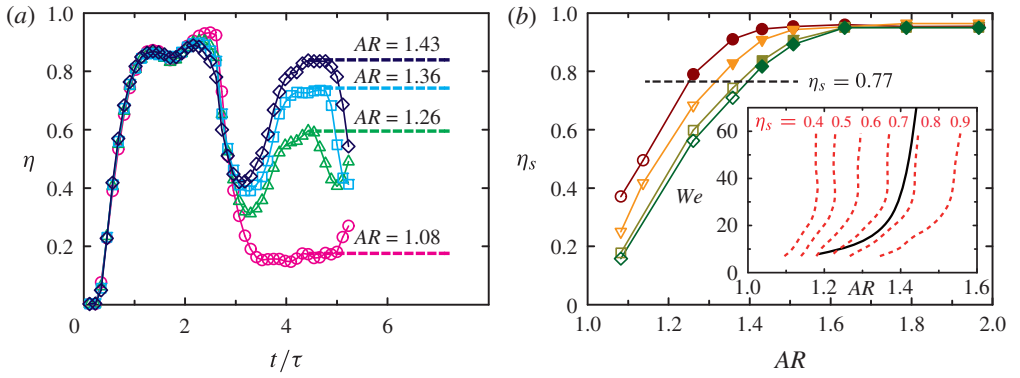


FIGURE 9. (Colour online) (*a*) Non-axial distribution of KE (η) as a function of time for different *AR*s and $We = 23$. Here η denotes the ratio of the non-axial KE to the total KE. Drops begin to spread at $t = 0$ and initiate axis switching at $3\tau < t < 5\tau$, where $\tau = D_0/U_0$. (*b*) The value of η measured at the axis-switching time (η_s) for various *AR*s and Weber numbers of 7 (○), 14 (▽), 23 (□), and 46 (◇); the open and filled symbols indicate the rebound case and deposition (rebound suppression) case, respectively. The inset represents the transition curve shown in figure 8(*b*) (solid line) and contour lines of η_s (dashed line).

As an additional note, we found dependence of the retraction rate on the Weber number for ellipsoidal drops. In the low-viscosity regime, the retraction rate of a spherical drop is independent of the impact velocity (Thoroddsen, Etoh & Takehara 2003; Bartolo, Josserand & Bonn 2005; Eggers *et al.* 2010). For ellipsoidal drops, in contrast, the retraction rate in the *y*-axis is independent of *We*, whereas the retraction rate in the *x*-axis increases with *We* (supplementary material, § S6). These findings may explain why the rebound/deposition transition is affected by the Weber number.

5. Conclusions

We have investigated the impact dynamics and outcomes of ellipsoidal drops as a function of the geometric *AR* and the Weber number by conducting experimental and numerical analyses. Experimental observation demonstrates the dominant effect of *AR* on impact behaviour and rebound suppression. We characterize the rebound case for low *AR* and the deposition case for high *AR* based on the liquid alignment along the *x*-axis and the consequent axis switching during retraction. The numerical analyses explain the experimental results of impact behaviour, thus indicating that the maximal extension for each axis is D_{my} (*y*-axis) $< D_m$ (spherical case) $< D_{mx}$ (*x*-axis) and that the discrepancies between the maximal extensions increase with *AR*.

Based on simple scaling analyses, the maximal extensions in the *x*-axis and the *y*-axis are estimated as functions of *AR* and *We*, which can sufficiently describe the spreading dynamics obtained in both experiment and simulation. The ratio of maximal extensions follows the scaling relation $D_{mx}/D_{my} \sim AR^{1/2}$, confirming a strong dependence on *AR* rather than on *We*. The rebound/deposition regimes are distinguished from each other when D_{mx}/D_{my} is close to 1.2. The transition diagram identifying the two regimes over *AR* and *We* domains shows that, once a drop keeps *AR* more than 1.35, rebound can be completely suppressed regardless of the value of *We* in the experiment. To understand the transition curves systematically, the non-axial distribution of KE at the axis-switching time has been introduced, which is interpreted

https://doi.org/10.1017/jfm.2014.332 Published online by Cambridge University Press

as the degree of axis switching during retraction. Rebound can be suppressed when the non-axial KE is higher than 77 % of the total KE at the axis-switching time.

Ellipsoidal drop impact can control the deposition of fluids, expanding the dynamics to three-dimensions. Without using additives or solid modification, the controllable drop shape can provide a convenient parameter in diverse applications, including surface patterning, cleaning, and cooling. Our future work will examine the effects of surface hydrophobicity and drop size on shape-dependent deposition.

Acknowledgements

This work was supported by the Mid-career Researcher Program through the National Research Foundation of Korea (NRF) grant funded by the Korean government (MSIP) (No. 2012R1A2A2A06047424).

Supplementary materials

Supplementary materials are available at http://dx.doi.org/10.1017/jfm.2014.332.

REFERENCES

ANTONINI, C., AMIRFAZLI, A. & MARENGO, M. 2012 Drop impact and wettability: from hydrophilic to superhydrophobic surfaces. *Phys. Fluids* **24**, 102104.

ANTONINI, C., VILLA, F., BERNAGOZZI, I., AMIRFAZLI, A. & MARENGO, M. 2013 Drop rebound after impact: the role of the receding contact angle. *Langmuir* **29**, 16045–16050.

AYTOUNA, M., BARTOLO, D., WEGDAM, G., BONN, D. & RAFAÏ, S. 2010 Impact dynamics of surfactant laden drops: dynamic surface tension effects. *Exp. Fluids* **48**, 49–57.

AZIZ, S. D. & CHANDRA, S. 2000 Impact, recoil and splashing of molten metal droplets. *Intl J. Heat Mass Transfer* **43**, 2841–2857.

BARTOLO, D., BOUDAOUD, A., NARCY, G. & BONN, D. 2007 Dynamics of non-Newtonian droplets. *Phys. Rev. Lett.* **99**, 174502.

BARTOLO, D., JOSSERAND, C. & BONN, D. 2005 Retraction dynamics of aqueous drops upon impact on non-wetting surfaces. *J. Fluid Mech.* **545**, 329–338.

BERGERON, V., BONN, D., MARTIN, J. Y. & VOVELLE, L. 2000 Controlling droplet deposition with polymer additives. *Nature* **405**, 772–775.

BIANCE, A.-L., CHEVY, F., CLANET, C., LAGUBEAU, G. & QUÉRÉ, D. 2006 On the elasticity of an inertial liquid shock. *J. Fluid Mech.* **554**, 47–66.

CHO, S. J., NAM, H., RYU, H. & LIM, G. 2013 A rubberlike stretchable fibrous membrane with anti-wettability and gas breathability. *Adv. Funct. Mater.* **23**, 5577–5584.

CLANET, C., BÉGUIN, C., RICHARD, D. & QUÉRÉ, D. 2004 Maximal deformation of an impacting drop. *J. Fluid Mech.* **517**, 199–208.

CROOKS, R., COOPER-WHITEZ, J. & BOGER, D. V. 2001 The role of dynamic surface tension and elasticity on the dynamics of drop impact. *Chem. Engng Sci.* **56**, 5575–5592.

DE GANS, B.-J., DUINEVELD, P. C. & SCHUBERT, U. S. 2004 Inkjet printing of polymers: state of the art and future developments. *Adv. Mater.* **16**, 203–213.

DENG, W. & GOMEZ, A. 2010 The role of electric charge in microdroplets impacting on conducting surfaces. *Phys. Fluids* **22**, 051703.

DENG, W. & GOMEZ, A. 2011 Electrospray cooling for microelectronics. *Intl J. Heat Mass Transfer* **54**, 2270–2275.

EGGERS, J., FONTELOS, M. A., JOSSERAND, C. & ZALESKI, S. 2010 Drop dynamics after impact on a solid wall: theory and simulations. *Phys. Fluids* **22**, 062101.

ENRIQUEZ, O. R., PETERS, I. R., GEKLE, S., SCHMIDT, L. E., LOHSE, D. & VAN DER MEER, D. 2012 Collapse and pinch-off of a non-axisymmetric impact-created air cavity in water. *J. Fluid Mech.* **701**, 40–58.

https://doi.org/10.1017/jfm.2014.332 Published online by Cambridge University Press

GATNE, K. P., JOG, M. A. & MANGLIK, R. M. 2009 Surfactant-induced modification of low Weber number droplet impact dynamics. *Langmuir* **25**, 8122–8130.

GUNJAL, P. R., RANADE, V. V. & CHAUDHARI, R. V. 2005 Dynamics of drop impact on solid surface: experiments and VOF simulations. *AIChE J.* **51**, 59–78.

KANNAN, R. & SIVAKUMAR, D. 2008 Drop impact process on a hydrophobic grooved surface. *Colloids Surf.* A **317**, 694–704.

KIM, J. 2007 Spray cooling heat transfer: the state of the art. *Intl J. Heat Fluid Flow* **28**, 753–767.

LAMB, H. 1945 *Hydrodynamics*, 6th edn. Dover Publications.

LEE, H. J. & KIM, H.-Y. 2004 Control of drop rebound with solid target motion. *Phys. Fluids* **16**, 3715–3719.

LEE, M. W., LATTHE, S. S., YARIN, A. L. & YOON, S. S. 2013 Dynamic electrowetting-on-dielectric (DEWOD) on unstretched and stretched Teflon. *Langmuir* **29**, 7758–7767.

LUNKAD, S. F., BUWA, V. V. & NIGAM, K. D. P. 2007 Numerical simulations of drop impact and spreading on horizontal and inclined surfaces. *Chem. Engng Sci.* **62**, 7214–7224.

MANGILI, S., ANTONINI, C., MARENGO, M. & AMIRFAZLI, A. 2012 Understanding the drop impact phenomenon on soft PDMS substrates. *Soft Matt.* **8**, 10045–10054.

MAO, T., KUHN, D. C. S. & TRAN, H. 1997 Spread and rebound of liquid droplets upon impact on flat surfaces. *AIChE J.* **43**, 2169–2179.

MARENGO, M., ANTONINI, C., ROISMAN, I. V. & TROPEA, C. 2011 Drop collisions with simple and complex surfaces. *Curr. Opin. Colloid Interface Sci.* **16**, 292–302.

MOUROUGOU-CANDONI, N., PRUNET-FOCH, B., LEGAY, F., VIGNES-ADLER, M. & WONG, K. 1997 Influence of dynamic surface tension on the spreading of surfactant solution droplets impacting onto a low-surface-energy solid substrate. *J. Colloid Interface Sci.* **192**, 129–141.

PASANDIDEH-FARD, M., QIAO, Y. M., CHANDRA, S. & MOSTAGHIMI, J. 1996 Capillary effects during droplet impact on a solid surface. *Phys. Fluids* **8**, 650–659.

RAYLEIGH, LORD 1879 On the capillary phenomena of jets. *Proc. R. Soc. Lond.* **29**, 71–97.

REYSSAT, M., PÉPIN, A., MARTY, F., CHEN, Y. & QUÉRÉ, D. 2006 Bouncing transitions on microtextured materials. *Europhys. Lett.* **74**, 306–312.

RIOBOO, R., MARENGO, M. & TROPEA, C. 2002 Time evolution of liquid drop impact onto solid, dry surfaces. *Exp. Fluids* **33**, 112–124.

RIOBOO, R., TROPEA, C. & MARENGO, M. 2001 Outcomes from a drop impact on solid surfaces. *Atomiz. Sprays* **11**, 155–165.

RIOBOO, R., VOUÉ, M., VAILLANT, A. & DE CONINCK, J. 2008 Drop impact on porous superhydrophobic polymer surfaces. *Langmuir* **24**, 14074–14077.

SMITH, M. I. & BERTOLA, V. 2010 Effect of polymer additives on the wetting of impacting droplets. *Phys. Rev. Lett.* **104**, 154502.

THORODDSEN, S. T., ETOH, T. G. & TAKEHARA, K. 2003 Air entrapment under an impacting drop. *J. Fluid Mech.* **478**, 125–134.

WIRTH, W., STORP, S. & JACOBSEN, W. 1991 Mechanisms controlling leaf retention of agricultural spray solutions. *Pest. Sci.* **33**, 411–420.

YARIN, A. L. 2006 Drop impact dynamics: splashing, spreading, receding, bouncing. . . . *Annu. Rev. Fluid Mech.* **38**, 159–192.

YUN, S., HONG, J. & KANG, K. H. 2013 Suppressing drop rebound by electrically driven shape distortion. *Phys. Rev.* E **87**, 033010.

ZANG, D., WANG, X., GENG, X., ZHANG, Y. & CHEN, Y. 2013 Impact dynamics of droplets with silica nanoparticles and polymer additives. *Soft Matt.* **9**, 394–400.

https://doi.org/10.1017/jfm.2014.332 Published online by Cambridge University Press